Available online at www.sciencedirect.com
ScienceDirect
Trans. Nonferrous Met. Soc. China 32(2022) 1910−1925
Transactions of Nonferrous Metals Society of China
www.tnmsc.cn

Formation mechanism and wear behavior of gradient nanostructured Inconel 625 alloy

Yu-bi GAO[1,2,3], Xiu-yan LI[4], Yuan-jun MA[1,2,4], Matthew KITCHEN[3], Yu-tian DING[1,2], Quan-shun LUO[3]

1. State Key Laboratory of Advanced Processing and Recycling of Non-ferrous Metals,
Lanzhou University of Technology, Lanzhou 730050, China;
2. School of Materials Science and Engineering, Lanzhou University of Technology, Lanzhou 730050, China;
3. Materials and Engineering Research Institute, Sheffield Hallam University, Sheffield, S1 1WB, UK;
4. Shenyang National Laboratory for Materials Science, Institute of Metal Research,
Chinese Academy of Sciences, Shenyang 110016, China

Received 19 May 2021; accepted 26 November 2021

Abstract: The formation mechanism and wear behavior of a gradient nanostructured (GNS) Inconel 625 alloy were investigated using SEM, TEM and ball-on-disc sliding wear tester. The results show that surface mechanical grinding treatment (SMGT) induced an approximately 800 μm-deep gradient microstructure, consisting of surface nano-grained, nano-laminated, nano-twined, and severely deformed layers, which resulted in a reduced gradient in micro-hardness from 6.95 GPa (topmost surface) to 2.77 GPa (coarse-grained matrix). The nano-grained layer resulted from the formation of high-density nano-twins and subsequent interaction between nano-twins and dislocations. The width and depth of the wear scar, wear loss volume, and wear rate of the SMGT-treated sample were smaller than those of untreated coarse-grained sample. Moreover, the wear mechanisms for both samples were mainly abrasive wear and adhesive wear, accompanied with mild oxidation wear. The notable wear resistance enhancement of the GNS Inconel 625 alloy was attributed to the high micro-hardness, high residual compressive stress, and high strain capacity of the GNS surface layer.

Key words: Inconel 625 alloy; surface mechanical grinding treatment; gradient nanostructure; formation mechanism; wear behavior; residual stress

---

1 Introduction

Inconel 625 alloy is a typical solid solution-strengthened nickel-based wrought superalloy, and is widely used in aeronautical, aerospace, chemical, petrochemical, and marine industries due to good combination of high yield strength, tensile strength, creep strength, excellent processability, and weldability and good resistance to high temperature corrosion on prolonged exposure to aggressive environments [1−4]. However, its widespread use has been limited as its microstructure and properties are highly sensitive to friction and wear. This makes the alloy poor resistant to friction and wear, causing premature failure. Therefore, improvements in the friction and wear resistance of the alloy have been sought through traditional surface modification techniques to extend its service lifetime. Numerous studies have been conducted to improve the wear resistance of Inconel 625 alloy through laser cladding [5,6], borotitanising [7], nitriding [8], and high-velocity oxy-fuel (HVOF) [9]. However, the thermal effect of these techniques induces

---

Corresponding author: Yu-tian DING, Tel: +86-13893243521, E-mail: dingyt@lut.edu.cn, dingyutian@126.com;
Quan-shun LUO, Tel: +44-1142253649, E-mail: q.luo@shu.ac.uk

DOI: 10.1016/S1003-6326(22)65918-1

destructive tensile residual stress in the surface layer of treated materials, which can substantially reduce fatigue strength and increase cracking susceptibility [10,11].

Recently, a novel surface nanocrystallization approach has been developed, which can be used to synthesize a gradient nanostructured (GNS) surface layer with residual compressive stresses on nickel-based superalloys through surface severe plastic deformation (SSPD). The resultant surfaces were reported to have enhanced resistances to wear, corrosion, and fatigue, as well as improved strength and ductility of the alloys without changes in their chemical composition [12−14]. For example, KUMAR et al [15] and BISHT et al [16] found an increase in the hardness of a surface nanostructured layer and an improvement in the wear resistance of Inconel 718 alloy after surface mechanical attrition treatment (SMAT). AMANOV and UMAROV [17] reported that the fretting wear resistance of Inconel 690 alloy was improved through combined local heat treatment (LHT) and ultrasonic nanocrystal surface modification (UNSM). This improvement was attributed to the improvement of mechanical properties, the increase of surface roughness, the formation of surface residual compressive stresses, and the presence of a nanostructured surface layer. In addition, VILLEGAS et al [18] reported the enhanced fatigue resistance of C-2000 superalloy through a surface nanocrystallization and hardening (SNH) process, which is related to surface nanocrystallization, work hardening, and residual compressive stresses. KUMAR et al [19] reported that the enhancement of the fatigue resistance of Inconel 718 alloy through SMAT was attributed to the positive influences of nanostructured layer, residual compressive stress, and work hardened layer. In addition, KUMAR et al [20] also found that the yield and tensile strengths of Inconel 718 alloy increased marginally by 3.5% and 2.15%, respectively, and the ductility was reduced by 3.4% following ultrasonic shot peening (USSP). DING et al [21] reported that surface mechanical grinding treatment (SMGT) of the NiCrMo-based C-22HS alloys generated a gradient surface microstructure consisting of surface nano-laminated (NL) layer, deformation twinned layer, and severely deformed layer. The abovementioned studies clearly indicated that the improved surface and global properties of nickel-based superalloys were closely related to the residual compressive stresses, microstructures, and the extent of strain hardening of surface nanostructured layer. In addition, these different characteristics also appeared in strain-induced layers of the alloys under different SSPD processes, which substantially depend on the stacking fault energy (SFE) and deformation conditions. For instance, pure Ni with high SFE (128 mJ/m^2) can form nano-laminated (NL) structures through dislocation slip during SMGT [22], whereas an Inconel 600 alloy with low SFE (28 mJ/m^2) can form nano-grained (NG) structures through the interaction of deformation twinning and dislocations during SMAT [23]. Nickel-based superalloys with low-to-medium SFE, such as NiCrMo-based C-22HS alloy, can form NL structures through dislocation slip during SMGT [21], whereas Hastelloy C-2000 alloy can form NG structures through the interaction of deformation twinning and dislocations during SNH process [19]. However, the formation mechanisms of GNS Inconel 625 alloy with low-to-medium SFE and the effect of gradient nanostructure on sliding wear behavior have not been systematically investigated.

In this work, a novel SSPD technique developed by LI et al [24], namely SMGT, was used to produce a GNS surface layer on the Inconel 625 rod at room temperature to investigate the effect of GNS on the wear behavior for Inconel 625 alloy under dry sliding. Firstly, the GNS characteristics of a SMGT-treated sample were investigated through micro-hardness distribution, cross-section morphology, and microstructure. Secondly, the effect of gradient nanostructure on the wear behavior of the alloy was investigated through surface and subsurface morphologies and microstructure of the wear scar. In addition, the formation mechanisms of GNS Inconel 625 alloy and the effect of gradient nanostructure on wear resistance were discussed.

2 Experimental

2.1 Materials

The materials used in the present work was an Inconel 625 alloy with the following nominal chemical composition (in mass fraction): 0.042% C, 21.77% Cr, 0.19% Co, 8.79% Mo, 0.21% Al, 0.40%

Ti, 3.68% Fe, 3.75% Nb, 0.12% Si, 0.20% Mn, 0.0006% S, 0.006% P, 0.06% Cu, and balanced Ni. The material was received in the form of a hot-extruded bar and was machined into rod samples with dimensions of 14 mm in diameter and 110 mm in length. The samples were solution heat-treated at 1150 °C for 1 h and then air-cooled to obtain homogeneous polycrystalline austenite microstructure with an average grain size of 110 μm and a micro-hardness of 2.77 GPa.

2.2 Surface mechanical grinding treatment (SMGT)

During the SMGT process, as schematically illustrated in Fig. 1(a), the bar sample rotated at a velocity v_1 with respect to a hemispherical WC−Co tool tip (with a radius of R=8 mm), which sides along the rod axis from the right to the left at a velocity v_2. With a preset penetration depth of the tool tip into the sample, a_p, a plastic deformation zone was induced underneath the tip, as shown in Fig. 1(b). The SMGT process parameters used in this work are listed in Table 1. The process was performed at room temperature, and a flowing cutting lubricant was supplied between the WC−Co ball and rod samples. Detailed information can be found in a previous research [24].

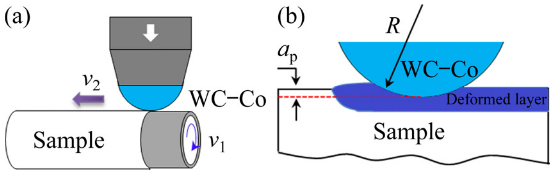

Fig. 1 Schematic illustration of SMGT set-up (a) and plastic deformation layer induced by tool tip (b)

Table 1 Parameters of SMGT process

Rotating velocity, v_1/(r·m^{-1})	Sliding velocity, v_2/(mm·min^{-1})	Indentation depth, a_p/μm	Number of repeated passes
300	6	30	10

2.3 Gradient nanostructure characterization

Surface roughness along the axial direction of the untreated and SMGT-treated samples was measured using an Alicona InfiniteFocus surface profilometer. Surface residual stress along the axial direction of the untreated and SMGT-treated samples was measured through X-ray diffraction (XRD) using a $\Omega-2\theta$ scan mode with Co K_α radiation on {311} plane as follows [25]:

$$d_{\{hkl\}}=\frac{1+\upsilon}{E}\sigma d_0\sin^2\psi_{\{hkl\}}+\frac{-2\upsilon}{E}\sigma d_0+d_0 \tag{1}$$

where σ is the residual stress. $d_{\{hkl\}}$ and d_0 are the lattice spacings of the selected diffraction peaks {311} of the Inconel 625 alloy with and without residual stress, respectively. For the XRD measurements, 11 fixed glancing angles at Ω=15°−95° were selected to scan the diffraction peak (311) in the range of 2θ=110°−114°, resulting in resultant off-axis angles of ψ from −40° to 40°, as shown in Fig. 2. E and υ are the elastic modulus and Poisson's ratio of the Inconel 625 alloy (205 GPa and 0.308), respectively. Using the measured lattice spacing d, derived from the diffraction angle 2θ using the Bragg equation, and the calculated ψ values ($\psi=\theta-\Omega$), the $d-\sin^2\psi$ linear regression was performed to calculate the residual stress.

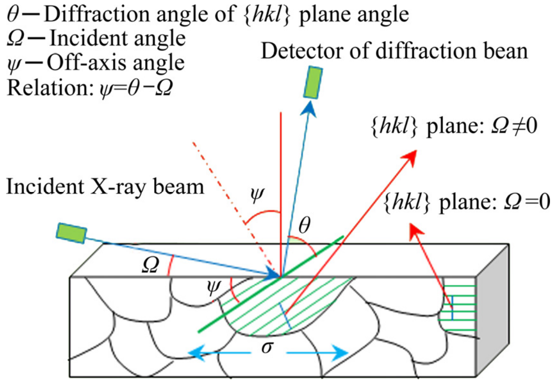

Fig. 2 Schematic diagram showing geometric set-up of X-ray diffraction (XRD) residual stress measurements

The surface and cross-sectional micro-hardness of the SMGT-treated samples was measured using the Duramin−40 micro-hardness tester. A Vickers diamond pyramid indenter was used to apply a 25 g load over a dwell time of 10 s. For the cross-sectional measurements, the indents were made approximately 20 μm apart, based on the ASTM E92 standard to eliminate plastic field interaction. Five measurements were performed to estimate the mean micro-hardness value and standard error.

The cross-sectional microstructure of the SMGT-treated samples was characterized using an FEI Verios 460 scanning electron microscope (SEM). The sample was mechanically polished and then electro-polished in an electrolyte of 90 vol.%

ethanol and 10 vol.% perchloric acid for 25 s to reveal the microstructure. The microstructure in the topmost surface layer was observed using a JEOL−2100F FEG transmission electron microscope (TEM) operated at 200 kV. The TEM samples were peeled off from the surface of the GNS samples and carefully ground to a thickness of 50 μm, followed by ion thinning of the thin foil samples using a Gatan 691 precision ion polishing system.

2.4 Sliding wear tests

The wear behavior of the untreated and SMGT-treated samples was investigated using a ball-on-disc sliding wear tester under dry condition at room temperature in air with a relative humidity of approximately 30%. A WC−Co sphere with a diameter of 6 mm was used as a sliding counterpart. The tests were carried out using a sliding stroke of 5 mm, a normal load of 5 N, and a sliding speed of 20 mm/s for a duration of 60 min. The schematic diagram of the experimental set-up is shown in Fig. 3. Profiles of worn surfaces were measured using an Alicona InfiniteFocus surface profilometer to determine the wear loss volume as $V=AL$ (where A refers to the worn area determined by its profile and L is the oscillating stroke). The cross-sectional micro-hardness of the untreated and SMGT-treated samples after wear was measured using an Anton Paar NTH^2 nano-indenter. The loading force, loading rate, unloading rate, and dwell time were 50 mN, 100 mN/min, 100 mN/min, and 10 s, respectively. Three measurements were performed to estimate the mean nano-hardness and standard error.

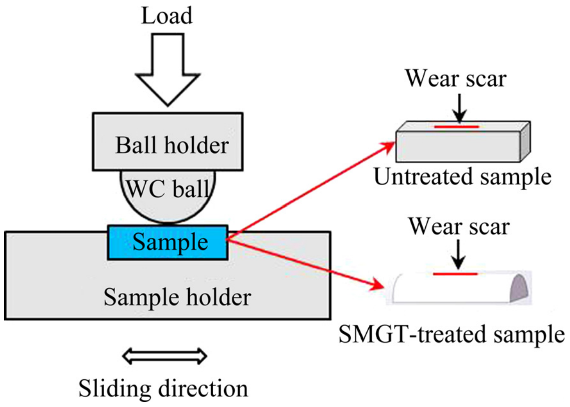

Fig. 3 Schematic illustration of ball-on-disc sliding wear test

2.5 Wear microstructure characterization

Worn samples were cleaned ultrasonically with ethanol for 5 min to investigate the worn surface morphology using an FEI Nova 200 SEM. Chemical analysis of the worn surface was performed using an energy dispersive spectrometer (EDS). Worn subsurface microstructure vertical to the sliding direction was characterized using an FEI Verios 460 SEM.

3 Results

3.1 Characterization of gradient nanostructure

3.1.1 Surface properties

Figure 4(a) shows the values of the surface roughness (R_a and R_z: R_a is the average roughness of the profile; R_z is the mean peak-to-valley height of roughness profile) of the untreated and SMGT-treated samples. It was found that the SMGT-treated sample had a higher surface roughness compared to the untreated coarse-grained (CG) sample. The surface residual compressive stresses of the untreated and SMGT-treated samples are shown in Fig. 4(b). The surface residual compressive stress increased by ~500 MPa after the SMGT treatment, which was believed to be caused by non-uniform plastic deformation in the surface layer during the process [26]. Figure 4(c) shows the values of the surface micro-hardness of the untreated and SMGT-treated samples. It can be seen that the SMGT treatment increased the surface micro- hardness due to grain refinement and strain hardening during the SMGT process. Overall, the surface of the SMGT-treated sample had a high roughness, residual compressive stress, and micro-hardness.

3.1.2 Micro-hardness gradient distribution

Figure 5 illustrates the variations in the average micro-hardness of both the SMGT-treated and the untreated samples at increasing depth from the surface into the bulk material. The micro-hardness of the treated top surface layer was approximately 6.95 GPa, which was 1.5 times higher than that of the CG matrix (2.77 GPa). The micro-hardness of the SMGT-treated sample decreased as the depth from the surface increased, obtaining a value similar to the untreated sample after reaching approximately 800 μm. This resulted in a hardness profile that was consistent with the microstructural characteristics observed in the gradient structure (GS) determined through SEM and TEM analyses.

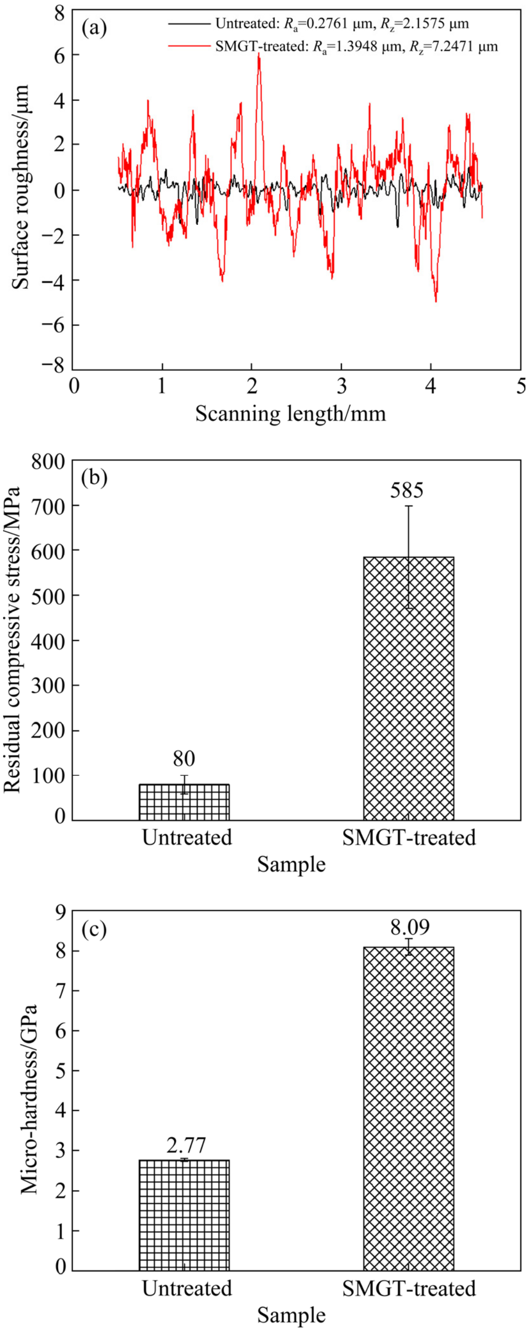

Fig. 4 Surface roughness (a), surface residual compressive stress (b) and surface micro-hardness (c) profiles of untreated and SMGT-treated samples

3.1.3 Microstructure of gradient nanostructure

Figure 6(a) showed that the microstructure of the untreated sample consisted of large coarse equiaxed grains and a few fine recrystallized grains. It is known that the solution treatment process after hot extrusion is accompanied by static recrystallization of deformed microstructure and subsequent grain growth [27]. It can be seen in Figs. 5 and 6(b) that the SMGT-treated sample contained deformed microstructures within approximately 800 μm from the treated surface. Within the first 100 μm from the surface, the microstructure was highly deformed, and the original grain boundaries (GBs) were hardly identifiable through SEM due to severe plastic deformation and microstructural refinement. TEM observations were used to further characterize the top surface layer of the SMGT-treated sample, focusing on the detailed microstructures at different depths, as shown in Fig. 6(b). The microstructures located below 100 μm (Fig. 6(c)) showed the high-density nano-twins (NTs) with an average twin thickness of 55 nm. The corresponding selected area electron diffraction (SAED) pattern indicated the twin relationship. As the depth decreased, the volume fraction of the deformed NTs gradually increased, whereas its thickness was gradually reduced. As shown in Fig. 6(d), the microstructure of the layer at approximately 80 μm depth showed parallel deformation NTs with a thickness of several tens of nanometers. The corresponding SAED pattern showed a superposition of two ⟨011⟩ diffraction patterns, which were symmetrical to each other with respect to the {111} plane, indicating that the observed lamellar structure consisted of alternate stacks of twins and matrix. In addition, high-density dislocation arrays or walls were observed inside some twin−matrix (T−M) lamellae. As the depth was further decreased, the T−M lamellae transformed gradually to lamellar structures without twin relationship, as shown in Fig. 6(f) and the corresponding SAED pattern. Statistical measurements indicated that the average

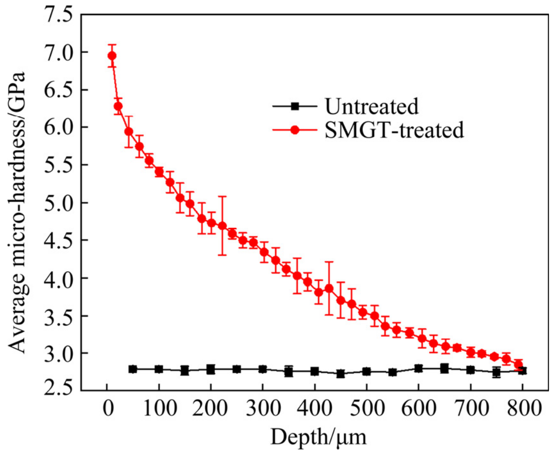

Fig. 5 Variations in average micro-hardness along depth direction of untreated and SMGT-treated samples

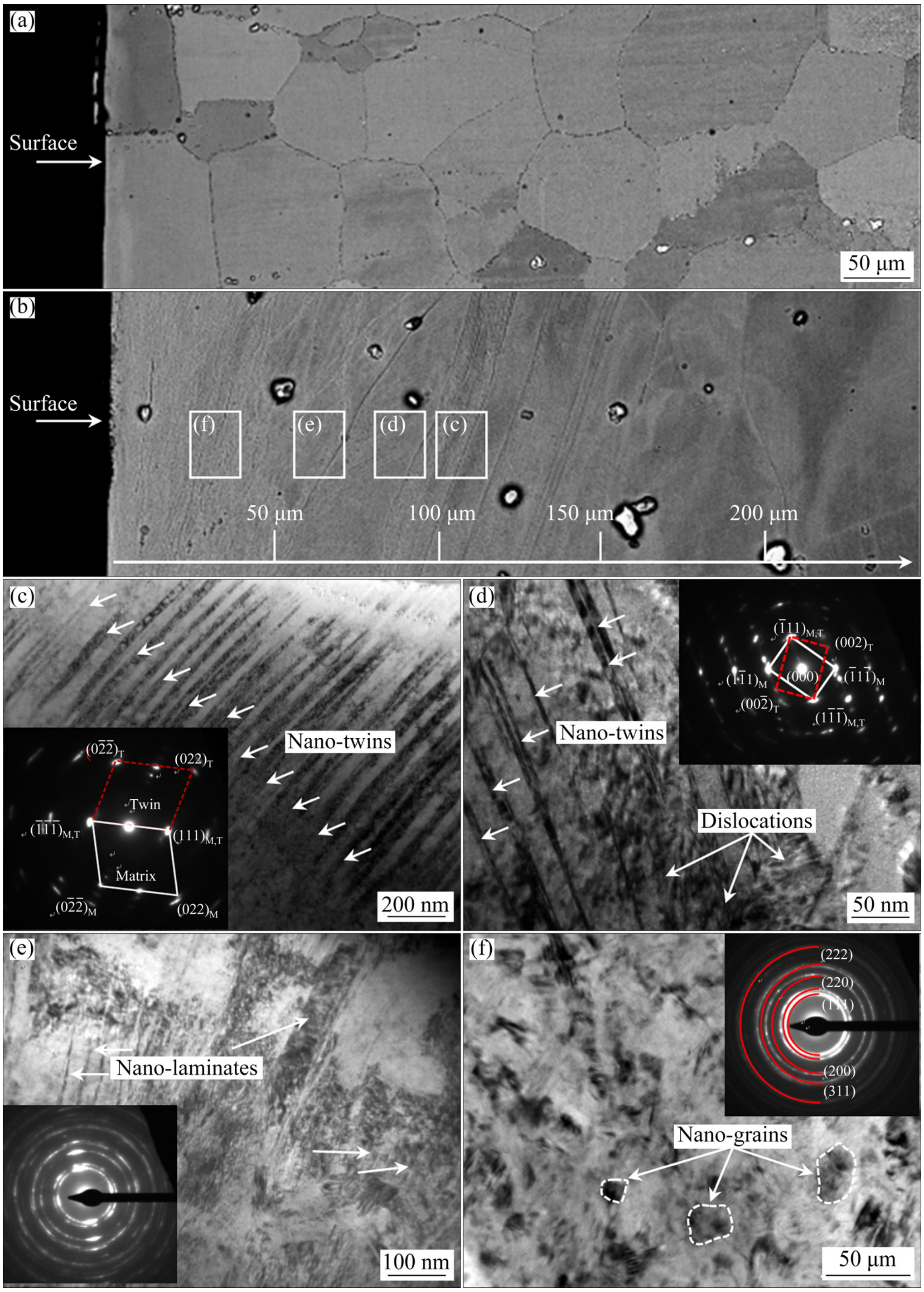

Fig. 6 Cross-sectional SEM images of untreated (a) and SMGT-treated (b) samples, and bright-filed TEM microstructures at different depths in surface layer of SMGT-treated sample: (c) ~100 μm; (d) ~80 μm; (e) ~60 μm; (f) ~30 μm (Insets in (c), (d), (e) and (f) show the corresponding SAED patterns)

lamellar thickness was approximately 42 nm at the depth of approximately 60 μm (Fig. 6(e)). The SAED pattern showed discontinuous diffraction rings with roughly six-folded symmetric distribution, specifically for (111) diffraction ring, implying that the NL structures had preferential orientation [22]. The NL structure characteristic has also been observed during the SMGT of NiCrMo-based C-22HS alloys [21]. In the top surface layer (~30 μm), nano-sized equiaxed grains with an average grain size of approximately 20 nm were observed. The corresponding SAED pattern (identified as a single-phase FCC structure) showed fairly uniform rings, indicating continuous and wide distribution of misorientations among the nano-grains (NG). A similar observation of nano-grains in the top surface layer of Inconel 600 alloy [23] and Inconel 718 alloy [15] after surface mechanical attrition treatment (SMAT) had been reported.

3.2 Sliding wear behavior

3.2.1 Basic tribological properties

Figure 7 shows the measured width and depth of wear scars, wear loss volumes, and wear rates of the untreated and SMGT-treated samples. As shown in Fig. 7(a), the wear scars of the SMGT-treated sample were shallower and narrower than those of the untreated sample. In addition, material pile-up at the two edges of the wear scar was evident in the SMGT-treated sample; however, that in the untreated sample was more significant. This provides a clear evidence of severe surface plastic deformation in the untreated sample. Similar wear scar profiles have been observed in the sliding wear of 316L [28] and 304 [29,30] stainless steels. As shown in Figs. 7(b) and (c), the measured wear loss volumes and wear rates of the SMGT-treated sample were reduced by 70% compared to the untreated sample under the same conditions. This indicates that SMGT may effectively improve the wear resistance of the Inconel 625 alloy.

3.2.2 Worn surface morphologies and wear mechanisms

The worn surfaces were observed using SEM to elucidate the predominant wear mechanisms. Figure 8 shows the SEM images and EDS analysis results of the worn surfaces of the untreated sample, in which the white double arrows indicated the sliding directions. As shown in Fig. 8(a), the width of the wear scar was approximately 860 μm, which is consistent with the measurements ((853±31) μm) shown in Fig. 7(a). A large number of intersecting slip lines appeared on the edge of the pile-up zone (Fig. 8(b)), indicating the occurrence of plastic deformation around the wear scar. Within the wear scar, a series of deep parallel grooves along the sliding direction were observed, resulting in a ploughing-like worn surface (Fig. 8(c)), which was caused mainly by abrasive wear mechanisms [31]. A few large lump-shaped particles were found adhered to the worn surface (Fig. 8(d)), suggesting that adhesive wear mechanisms were also present. EDS linear analysis (Fig. 8(e)) of these particles found that they were rich in oxygen with a slight depletion of both nickel and chromium. This indicates that the wear debris trapped between the tribo-pair could be broken into sufficiently small sizes and rapidly oxidized owing to their large exposed surface area under reciprocating sliding. The oxidation process is also accelerated by

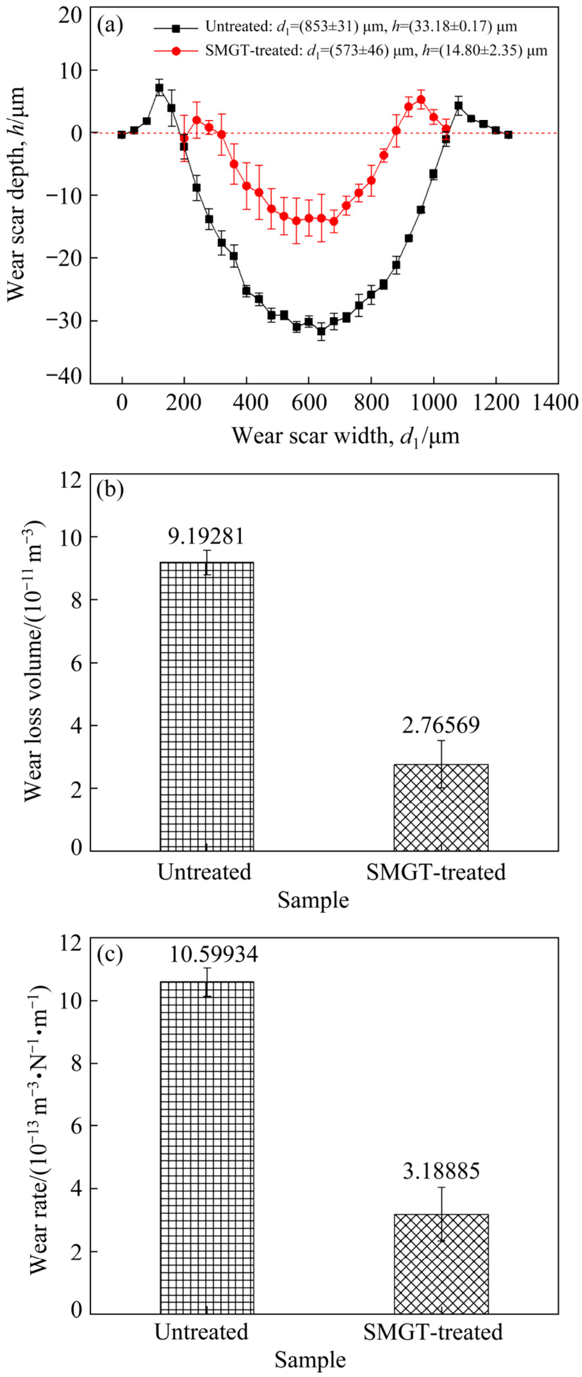

Fig. 7 Surface profiles of wear scar depth (a), wear loss volume (b) and wear rate (c) of samples in untreated and SMGT-treated conditions

frictional heat, high defect densities, and surface energy induced by sliding contacts [32]. In addition, the oxidized wear debris could serve as third-bodies that can reduce wear volume and wear rate by accommodating the speed between contacting surfaces [33]. Thus, the wear mechanisms of the untreated sample were mainly abrasive wear and adhesive wear, accompanied with mild oxidation wear.

Figure 9 shows the SEM images and EDS analysis results of the worn surfaces of the SMGT-treated sample. Analysis of the wear scar showed that it was approximately 580 μm wide, as shown in Fig. 9(a), which is consistent to the measurements ((573±46) μm) shown in Fig. 7(a). The wear scar was covered with fine particulate wear debris (Fig. 9(a)). During repetitive sliding, fine wear debris neither cuts nor prevents metal-to-metal contact, allowing adhesive wear to occur [34]. A large plate-like particle was observed on the worn surface, which had several cracks (Fig. 9(c)). This particle was probably formed through the agglomeration of a large number of fine wear particles, which joined together when they were subjected to large plastic strain and friction heat during reciprocating sliding. As shown in Fig. 9(b), the worn surface had shallow parallel wear grooves in the sliding direction, whereas the edge of the pile-up zone showed no slip lines. This indicates that the GNS Inconel 625 alloy resisted damage caused by plastic deformation and abrasion more effectively. In addition, oxidation wear was evident through EDS linear analysis of the wear debris (Fig. 9(e)), which was similar to the untreated sample (Fig. 8(e)). Thus, the wear mechanisms of the SMGT-treated sample were mainly adhesive wear and abrasive wear, accompanied with mild oxidation wear.

In addition, the EDS point analysis results of the oxygen content in the wear debris and worn surfaces of both the untreated and SMGT-treated samples are listed in Table 2. The oxygen content of the untreated sample was higher than that of the SMGT-treated sample, both in the wear debris and on the worn surface. This shows that the SMGT-treated sample had a better oxidation resistance during dry sliding wear than the untreated sample. However, the SMGT-treated sample did not change the wear mechanisms of the Inconel 625 alloy, which were mainly abrasive wear and adhesive wear, accompanied with mild oxidation wear.

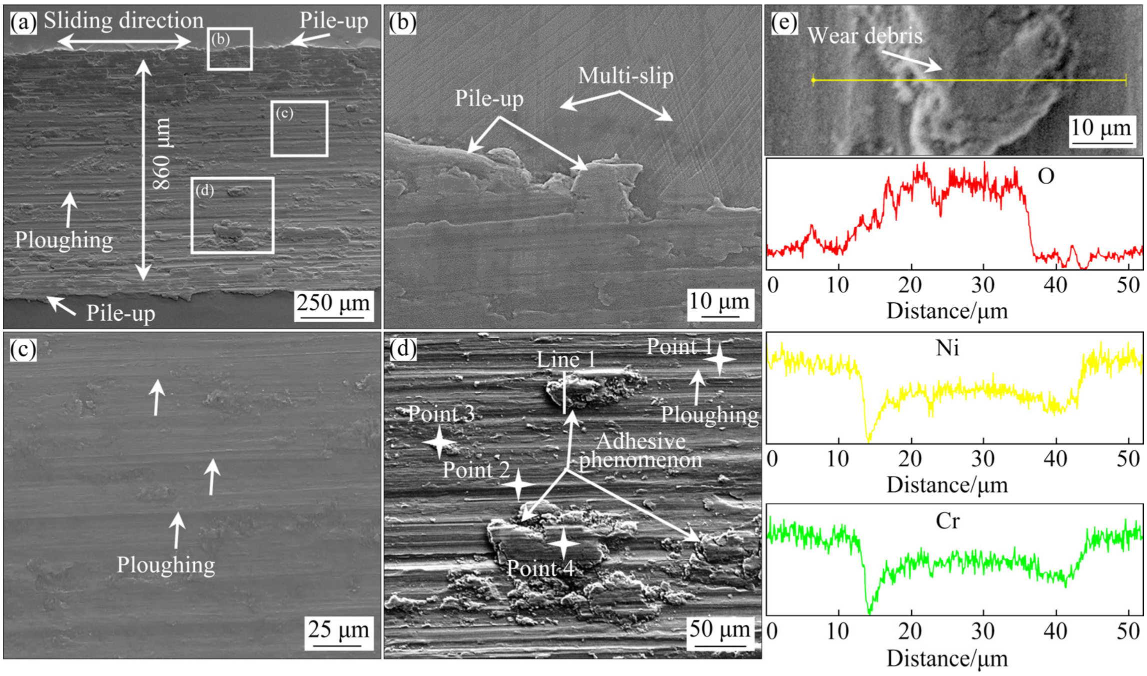

Fig. 8 SEM images and EDS analysis results of worn surfaces in untreated sample: (a) Surface morphology of wear scar; (b−d) Locally enlarged images in Fig. 8(a); (e) EDS line analysis results of wear debris in Fig. 8(d) (Points 1 and 2 correspond to EDS point analysis of worn surface in Fig. 8(d), and Points 3 and 4 correspond to EDS point analysis of wear debris in Fig. 8(d))

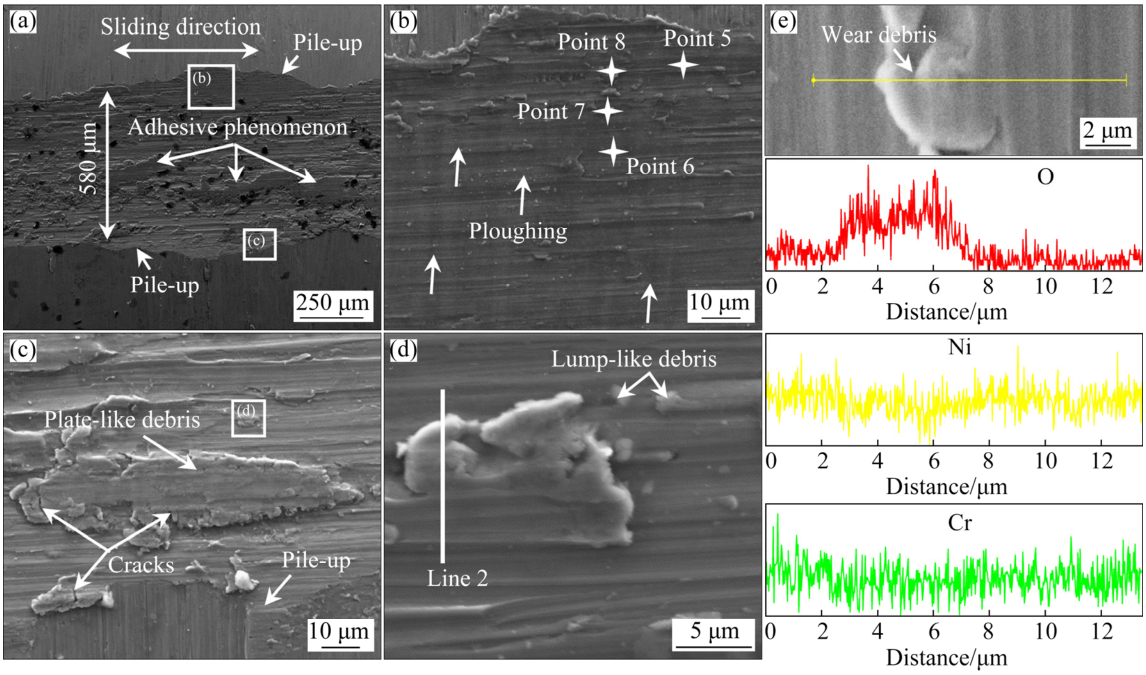

Fig. 9 SEM images and EDS analysis results of worn surfaces in SMGT-treated sample: (a) Wear scar surface morphology; (b−d) Locally enlarged images for Figs. 9(a) and (c), respectively; (e) EDS line analysis results of wear debris in Fig. 9(d) (Points 5 and 6 correspond to EDS point analysis of worn surface in Fig. 9(b), and Points 7 and 8 correspond to EDS point analysis of wear debris in Fig. 9(b))

Table 2 Comparison of EDS point analysis results of oxygen contents for wear debris and worn surface in untreated and SMGT-treated samples

Location	Untreated sample		SMGT-treated sample	
	Position	O content/wt.%	Position	O content/wt.%
Worn surface	Point 1	1.21	Point 5	0.76
	Point 2	1.25	Point 6	1.00
Wear debris	Point 3	11.30	Point 7	5.01
	Point 4	19.84	Point 8	4.10

3.2.3 Worn subsurface microstructure

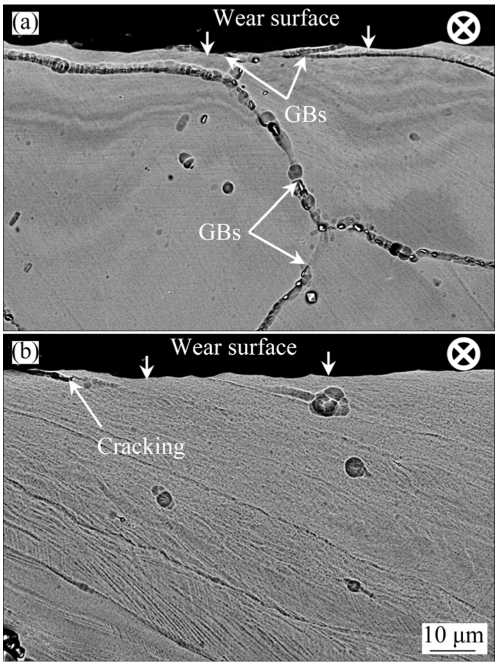

Fig. 10 Typical SEM images of worn subsurface microstructures for untreated (a) and SMGT-treated (b) samples (White circles indicate sliding direction)

Figure 10 shows the subsurface microstructures of the wear scars of the untreated (Fig. 10(a)) and SMGT-treated (Fig. 10(b)) samples. As shown in Fig. 10(a), interconnected GBs were observed on the worn surface and subsurface of the untreated sample. These GBs provide channels for crack initiation and propagation during sliding wear, resulting in high wear loss volume during the running-in stage. As shown in Fig. 10(b), cracks were observed on the worn surface with no cracks being found on the worn subsurface of SMGT-treated sample. In the SMGT-treated sample, the high hardness and residual compressive stress of the surface layer suppressed the crack initiation and propagation on the subsurface during slid wear, resulting in lower wear loss volume in the running-in stage. This suggests that residual compressive stress could significantly improve the wear resistance of Inconel 625 alloy.

Figures 11 and 12 show the cross-sectional SEM images of the microstructure of the untreated and SMGT-treated samples after sliding wear tests, respectively. As shown in Fig. 11(a), the width and depth of the wear scars were 862 and 33.51 μm, respectively, consistent with the profilometry measurements (Fig. 7(a)). The variations in the cross-section micro-hardness along depth of the untreated sample after wear tests (Fig. 13(a)) showed that the alloy had a significant deformed layer after the sliding wear tests, and the thickness of which was approximately 20 μm (Fig. 11(c)). In addition, the micro-hardness of the topmost surface of the alloy was 8.02 GPa, indicating that surface nanocrystallization occurred in the untreated sample after the sliding wear tests. According to the Schmid's law, slip deformation occurred preferentially on grains with soft orientation under loading, with slip lines parallel to the shear stress direction, as shown in Fig. 11(d). The results indicate that sliding wear-induced surface grain refinement occurred in the untreated sample during dry sliding wear tests.

SEM measurements of the wear scar of the SMGT-treated sample after sliding wear tests (Fig. 12(a)) showed that the scar had a width of 585 μm and a depth of 14.28 μm, consistent with the profilometry measurements (Fig. 7(a)). Variations in the cross-section micro-hardness along the depth of the SMGT-treated sample after the wear tests (Fig. 13(b)) showed that the alloy had a significant grain coarsening layer in the topmost surface layer after the sliding wear tests, and the thickness of which was approximately 15 μm (Fig. 12(c)). Moreover, the SMGT-induced GNS layer (NG/UFG layer, deformed twin layer and severe deformed layer) remained beneath the grain coarsening layer. In addition, the annealed twin boundaries in the severe deformation layer were bent, as shown in Fig. 12(b). The results indicate that sliding wear-induced surface nano-grain coarsening occurred in the SMGT-treated sample during the dry sliding wear tests.

4 Discussion

4.1 Formation mechanism of gradient nanostructure

Generally, the deformation of microstructures and grain refinement in CG metals and alloys, with an FCC structure, during plastic deformation, are closely associated with their SFE and deformation

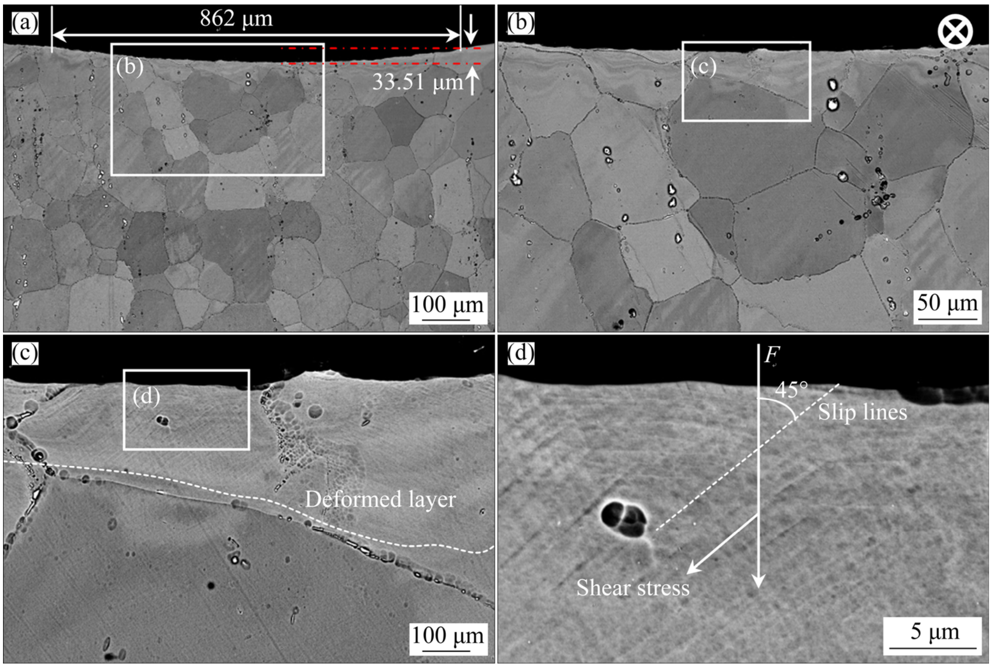

Fig. 11 SEM images of microstructure of untreated sample after sliding wear tests: (a) Cross-section microstructure of wear scar; (b) Locally enlarged image for Fig. 11(a); (c) Locally enlarged image for Fig. 11(b); (d) Locally enlarged image for Fig. 11(c) (White circle indicates sliding direction)

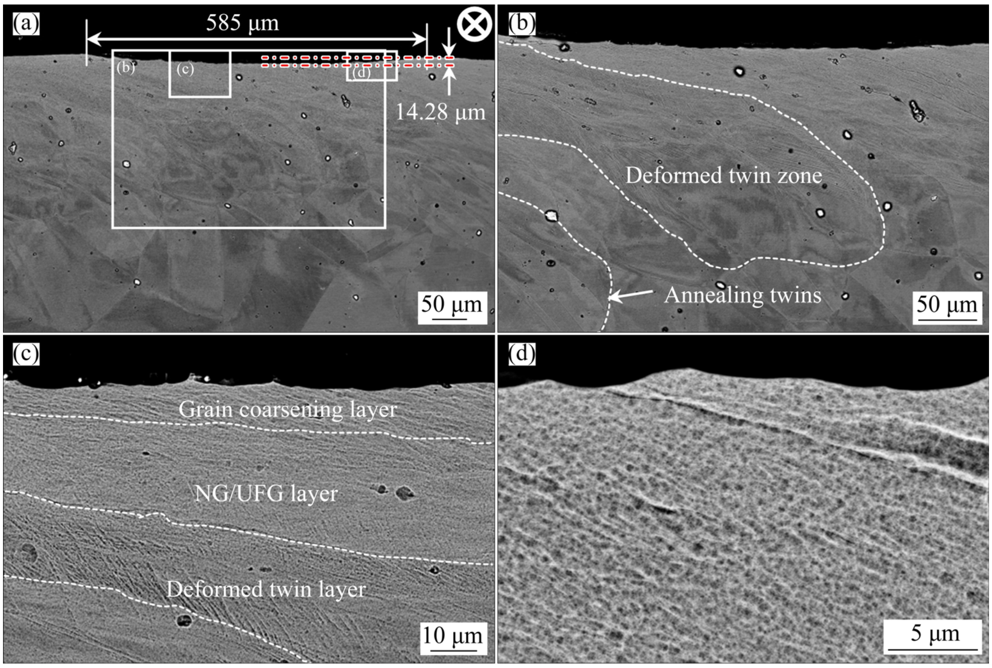

Fig. 12 SEM images of microstructure of SMGT-treated sample after sliding wear tests: (a) Cross-section microstructure of wear scar; (b−d) Locally enlarged images for Fig. 12(a) (White circle indicates sliding direction)

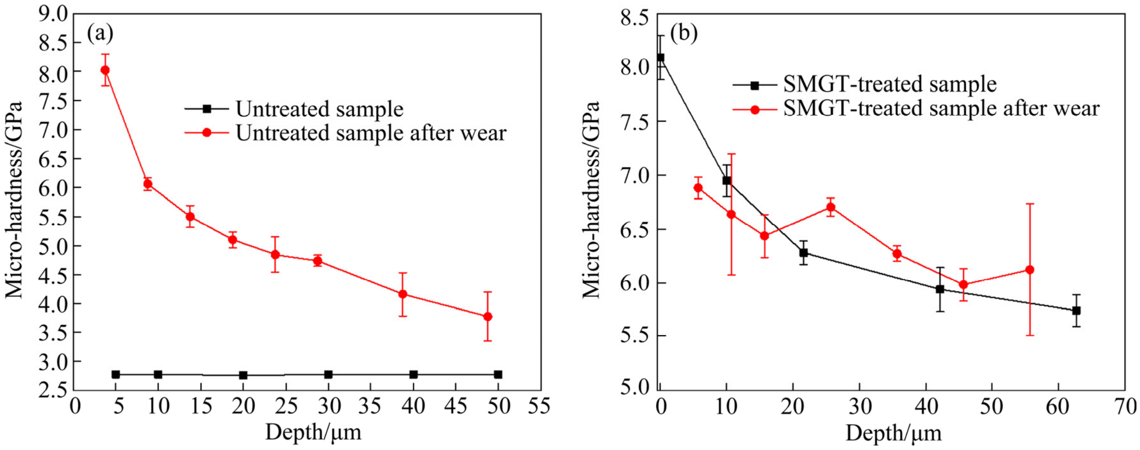

Fig. 13 Variations of average micro-hardness along depth direction of untreated (a) and SMGT-treated (b) samples after wear tests

conditions (such as strain, strain rate, and temperature) [35]. It is well known that during plastic deformation, metals and alloys with high SFE are deformed through dislocation slip, whereas metals and alloys with low SFE are deformed through twinning. In metals and alloys with intermediate SFE, deformation occurs through twinning at high strain rates and/or at low temperatures. However, at low strain rates and/or high deformation temperatures, dislocation slip is favored [36]. Therefore, the critical shear stress for twinning decreases as SFE decreases. However, the SMGT process produces inhomogeneous plastic deformation, resulting in gradient distributions of deformation strain and strain rate from the surface layer down to a certain depth in the bulk metal. This induces varying degrees of deformation and grain refinement at different depths, resulting in different deformation mechanisms of corresponding layers and a gradient distribution of the grain size [37].

In the present work, the Inconel 625 alloy had a chemical composition similar to that of the Inconel 600 alloy (Cr 15.72%, Fe 8.63%, Si 0.18%, Mn 0.16%, C 0.078%, Al 0.06%, Cu 0.04%, S <0.001%, and balanced Ni). The Inconel 600 alloy had an extremely low SFE (28 mJ/m^2) [38], and thus it is believed that the SFE of the Inconel 625 alloy was more likely to be in the low-to-medium range. Therefore, the deformation mechanism was through dislocation slip ({111}⟨110⟩) and twinning ({111}⟨112⟩) through the common deformation modes. In the low strain and strain rate regions, the shear stress reached or exceeded the critical shear stress necessary for dislocation ship. Thus, dislocation multiplication and dislocation tangle created numerous strip-shaped geometrically necessary dislocation (GND) boundaries, and these GND boundaries divided the original CGs into sub-grains [39]. As the strain and strain rate were increased, the dislocation cross-slip was suppressed, and the critical shear stress for twin formation was exceeded, where the passage of Shockley partial dislocations on successive slip {111} planes led to twinning [40]. Thus, twinning was the dominant deformation mode in this region. The formation of high-density deformation twins introduced a large number of TBs that subdivided the original CGs into T−M lamellae [41]. Localized deformation occurred in the form of shear bands (SBs) when further strain hardening became difficult. The shear strain twisted the TBs and led to the formation of randomly oriented NL structures within the SBs [21]. As the strain further increased, the interaction between dislocations and TBs and the NL boundaries induced further deformation and refinement of the NL structures, which eventually made equiaxed NG with random orientations formed [23,42,43].

TEM observations of the SMGT-treated sample (Fig. 6) indicated that the SMGT-induced surface NG layer was due to the formation of high-density NTs and the subsequent interaction between the NTs and dislocations. The NL boundaries also induced further deformation and refinement of the NL structures, which eventually made nano-scale equiaxed grains formed. It was found that the SMGT-induced gradient microstructure of the Inconel 625 alloy consisted of several layers, including surface NG, NL, NT, and severely deformed layers. The SMGT-induced gradient microstructure of the NiCrMo-based C-22HS alloy consisted of a surface NL layer, a deformation twinned layer, and severely deformed layers [21]. The presence of the SMGT-induced GNS layer in the superalloy was therefore related to the SFE of the material and the SMGT process parameters.

4.2 Sliding wear-induced plastic deformation

Sliding wear-induced plastic deformation is a surface severe plastic deformation process that refines grain and nanostructures to micrometer depths beneath the worn surface, similar to the SMGT process [44,45]. Different characteristics appeared in the surface layers with different SMGT and sliding wear-induced process parameters. In the untreated CG sample, the tangential shear force induced by sliding contact tended to plastically deform the near-surface materials during dry sliding wear. In the early stages of the wear, a large number of dislocations were created in the CGs. The shear strain increased with increasing repeated sliding passes, resulting in dislocation multiplication and formation of dislocation tangle from massive high-density dislocation walls (DWs) and subdivision of the original CGs into sub-grains [46]. As the shear stress accumulated, sub-grain boundaries evolved into high-angle grain boundaries, which subdivided the original CGs into NGs, as shown in Fig. 14(a). In the SMGT-treated sample, the topmost surface layer microstructure was equiaxed NGs, and grain coarsening occurred as a result of the grain boundary motion caused by the thermal-mechanical effect of frictional heating and friction forces during dry sliding wear, as shown in Fig. 14(b). Typical sliding wear-induced grain refinement and grain coarsening occurred in the worn subsurface of the microcrystalline and nanocrystalline Ni, respectively, during sliding wear tests [47].

The dry sliding wear was found to induce surface deformation in materials with a CG structure (Fig. 11), whereas, in materials with a NG structure, surface grain coarsening occurred (Fig. 12). In the untreated sample, the deformed layer could not accommodate the large plastic strain imposed by the friction force, thereby elongating the grains in the subsurface, which caused crack propagation channels, leading to low wear resistance. In contrast, the grain coarsening observed in the SMGT-treated samples accommodated the large plastic strain, thereby suppressing strain locations and crack propagations effectively, resulting in a significantly enhanced wear resistance.

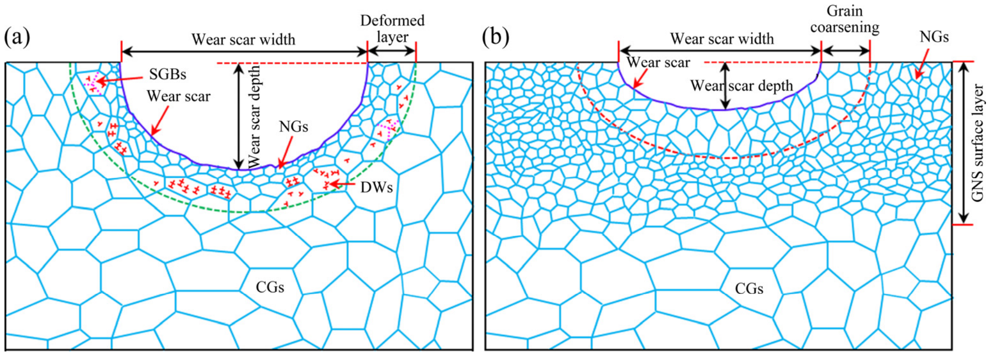

Fig. 14 Schematic diagrams showing cross-section of wear-induced plastic deformation in CGs (a) and NGs (b) during dry sliding wear

4.3 Effect of GNS surface layers on wear behavior

In this study, the GNS surface layer of the SMGT-treated sample generally had higher hardness and residual compressive stress compared to that of the untreated CG sample. Based on the Archard equation [48], the relationship between hardness (H) and wear rate (w) is

$$w = K\frac{P}{H} \tag{2}$$

where K is a pre-factor relative to the material's ductility, and P is the applied load. As described by Eq. (2), the wear rate w decreases with an increase in hardness (H) under a certain applied load. An empirical equation based on the Archard and Hall−Petch equations was used to describe the effect of grain refinement on wear rate w under unlubricated sliding conditions [49]:

$$w = w_0 + K\frac{P}{H_0 + kd_2^{-1/2}} \tag{3}$$

where w_0 represents the grain-size independent component of the wear rate, d_2 is the average grain size, and H_0 and k are materials constants. The abovementioned results indicate that the enhancement of the wear resistance was associated with the increase in micro-hardness, which was attributed to grain refinement. In addition, the residual compressive stress in the SMGT-treated sample delayed crack initiation and reduced crack propagation velocity after crack nucleation [50−52]. As seen in Figs. 4 and 7, the top surface of the GNS surface layer exhibited high micro-hardness and high residual compressive stress corresponding to the low wear loss volume and wear rate. Thus, the high micro-hardness and high compressive residual stress significantly improved the wear resistance of the Inconel 625 alloy.

5 Conclusions

(1) SMGT induced an approximately 800 μm deep gradient microstructure, consisted of surface nano-grained (NG), nano-laminated (NL), nano-twined (NT) and severely deformed layers, which resulted in a reduced gradient in micro-hardness from 6.95 GPa in the topmost surface to 2.77 GPa in the coarse grained (CG) matrix. In addition, the surface NG layer resulted from the formation of high-density nano-twins and subsequent interaction between nano-twins and dislocations.

(2) The width and depth of the wear scar, wear loss volume, and wear rate of the SMGT-treated sample were smaller than those of the untreated CG sample. In addition, the SMGT treatment did not change the wear mechanisms of the Inconel 625 alloy, which were mainly abrasive wear and adhesive wear, accompanied with mild oxidation wear.

(3) The grain refinement induced by sliding wear occurred in the untreated CG sample, whereas the grain coarsening induced by sliding wear occurred in the SMGT-treated sample.

(4) The GNS Inconel 625 alloy exhibited a significantly enhanced wear resistance compared to the untreated CG sample, owing to the high micro-hardness, high residual compressive stress, and high strain capacity of the GNS surface layer, which reduced the wear loss volume and wear rate.

Acknowledgments

This work was financially supported by the

National Key Research and Development Program of China (No. 2017YFA07007003), the National Natural Science Foundation of China (No. 51661019), the Program for Major Projects of Science and Technology in Gansu Province, China (No. 145RTSA004), the Hongliu First-class Discipline Construction Plan of Lanzhou University of Technology, China, the Incubation Program of Excellent Doctoral Dissertation, Lanzhou University of Technology, China, the Lanzhou University of Technology Excellent Students Studying Abroad Learning Exchange Fund, and the State Key Laboratory of Cooperation and Exchange Fund. Mr Leon BOWEN is acknowledged for his support in the transmission electron microscopy experiments in the University of Durham, United Kingdom.

References

[1] SHANKAR V, RAO K B S, MANNAN S L. Microstructure and mechanical properties of Inconel 625 superalloy [J]. Journal of Nuclear Materials, 2001, 288: 222−232.

[2] KUMAR A, RAJKUMAR K V, JAYAKUMAR T, RAJ B, MISHRA B, MISHRA B. Ultrasonic measurements for in-service assessment of wrought Inconel 625 cracker tubes of heavy water plants [J]. Journal of Nuclear Materials, 2006, 350: 284−292.

[3] MATHEW M D, PARAMESWARAN P, RAO K B S. Microstructural changes in alloy 625 during high temperature creep [J]. Materials Characterization, 2008, 59: 508−513.

[4] SAFARZADE A, SHARIFITABAR M, SHAFIEE AFARANI M. Effects of heat treatment on microstructure and mechanical properties of Inconel 625 alloy fabricated by wire arc additive manufacturing process [J]. Transactions of Nonferrous Metals Society of China, 2020, 30: 3016−3030.

[5] FENG Kai, CHEN Yuan, DENG Ping-shun, LI Yu-yan, ZHAO Hai-xing, LU Feng-gui, LI Rui-feng, HUANG Jian, LI Zhu-guo. Improved high-temperature hardness and wear resistance of Inconel 625 coatings fabricated by laser cladding [J]. Journal of Materials Processing Technology, 2017, 243: 82−91.

[6] DENG Ping-shun, YAO Cheng-wu, FENG Kai, HUANG Xinag-xiang, LI Zhu-guo, LI Yu-yan, ZHAO Hai-xing. Enhanced wear resistance of laser cladded graphene nanoplatelets reinforced Inconel 625 superalloy composite coating [J]. Surface and Coatings Technology, 2018, 335: 334−344.

[7] GÜNEN A, KANCA E, ÇAKIR H, KARAKAŞ M S, CÖK M S, KÜÇÜK Y, DEMIR M. Effect of borotitanizing on microstructure and wear behaviour of Inconel 625 [J]. Surface and Coatings Technology, 2017, 311: 374−382.

[8] BOROWSKI T, BROJANOWSKA A, KOST M, GARBACZ H, WIERZCHOŃ T. Modifying the properties of the Inconel 625 nickel alloy by glow discharge assisted nitriding [J]. Vacuum, 2009, 83: 1489−1493.

[9] LIU Z, CABRERO J, NIANG S, AL-TAHA Z Y. Improving corrosion and wear performance of HVOF-sprayed Inconel 625 and WC-Inconel 625 coatings by high power diode laser treatments [J]. Surface and Coatings Technology, 2007, 201: 7149−7158.

[10] ZHOU Sheng-fend, ZENG Xiao-yan, HU Qian-wu, HUANG Yong-jun. Analysis of crack behavior for Ni-based WC composite coatings by laser cladding and crack-free realization [J]. Applied Surface Science, 2008, 255: 1646−1653.

[11] de OLIVEIRA U, OCELÍ K V, de HOSSON J T M. Residual stress analysis in Co-based laser clad layers by laboratory X-rays and synchrotron diffraction techniques [J]. Surface and Coatings Technology, 2006, 201: 533−542.

[12] VILLEGAS J C, DAI K, SHAW L L, LIAW P K. Nanocrystallization of a nickel alloy subjected to surface severe plastic deformation [J]. Materials Science and Engineering A, 2005, 410: 257−260.

[13] ORTIZ A L, TIAN J W, VILLEGAS J C, SHAW L L, LIAW P K. Interrogation of the microstructure and residual stress of a nickel-base alloy subjected to surface severe plastic deformation [J]. Acta Materialia, 2008, 56: 413−426.

[14] VILLEGAS J C, SHAW L L. Nanocrystallization process and mechanism in a nickel alloy subjected to surface severe plastic deformation [J]. Acta Materialia, 2009, 57: 5782−5795.

[15] KUMAR S A, RAMAN S G S, SANKARA NARAYANAN T S N, GNANAMOORTHY R. Fretting wear behaviour of surface mechanical attrition treated alloy 718 [J]. Surface and Coatings Technology, 2012, 206: 4425−4432.

[16] BISHT A, GADDAM S, KUMAR L, DILEEP B L, SUWAS S. Precipitation behavior of IN718 after surface mechanical attrition treatment and its effect on wear properties [J]. JOM, 2018, 70: 2667−2676.

[17] AMANOV A, UMAROV R. The effects of ultrasonic nanocrystal surface modification temperature on the mechanical properties and fretting wear resistance of Inconel 690 alloy [J]. Applied Surface Science, 2018, 441: 515−529.

[18] VILLEGAS J C, SHAW L L, DAI K, YUAN W, TIAN J, LIAW P K, KLARSTROM D L. Enhanced fatigue resistance of a nickel-based Hastelloy induced by a surface nanocrystallization and hardening process [J]. Philosophical Magazine Letters, 2005, 85: 427−438.

[19] KUMAR S A, RAMAN S G S, NARAYANAN T S N S. Effect of surface mechanical attrition treatment on fatigue lives of Alloy 718 [J]. Transactions of the Indian Institute of Metals, 2012, 65(5): 473−477.

[20] KUMAR S, RAO G S, CHATTOPADHYAY K, MAHOBIA G S, SRINIVAS S N C, SINGH V. Effect of surface nanostructure on tensile behaviour of superalloy IN718 [J]. Materials and Design, 2014, 62: 76−82.

[21] DING J, LI Q, LI J, XUE S, FAN Z, WANG H, ZHANG X.

Mechanical behavior of structurally gradient nickel alloy [J]. Acta Materialia, 2018, 149: 57−67.

[22] LIU X C, ZHANG H W, LU K. Formation of nano-laminated structure in nickel by means of surface mechanical grinding treatment [J]. Acta Materialia, 2015, 96: 24−36.

[23] TAO N R, WU X L, SUI M L, LU J, LU K. Grain refinement at the nanoscale via mechanical twinning and dislocation interaction in a nickel-based alloy [J]. Journal of Materials Research, 2004, 19: 1623−1629.

[24] LI W L, TAO N R, LU K. Fabrication of a gradient nano-micro-structured surface layer on bulk copper by means of a surface mechanical grinding treatment [J]. Scripta Materialia, 2008, 59: 546−549.

[25] LUO Q, JONES A H. High-precision determination of residual stress of polycrystalline coatings using optimised XRD-sin 2ψ technique [J]. Surface and Coatings Technology, 2010, 205: 1403−1408.

[26] TAO N R, LU J, LU K. Surface Nanocrystallization by surface mechanical attrition treatment [J]. Materials Science Forum, 2008, 579: 91−108.

[27] BAILEY J E, HIRSCH P B. The recrystallization process in some polycrystalline metals [J]. Proceedings of the Royal Society A, 1962, 267: 11−30.

[28] WANG Yan-yan, YUE WEN, SHE Ding-shun, FU Zhi-qaing, HUANG Hai-peng, LIU Jia-jun. Effects of surface nanocrystallization on tribological properties of 316L stainless steel under MoDTC/ZDDP lubrications [J]. Tribology International, 2014, 79: 42−51.

[29] SUN Y. Sliding wear behaviour of surface mechanical attrition treated AISI 304 stainless steel [J]. Tribology International, 2013, 57: 67−75.

[30] SUN Y, BAILEY R. Improvement in tribocorrosion behavior of 304 stainless steel by surface mechanical attrition treatment [J]. Surface and Coatings Technology, 2014, 253: 284−291.

[31] SHANTHI M, LIM C Y H, LU L. Effects of grain size on the wear of recycled AZ91 Mg [J]. Tribology International, 2007, 40: 335−338.

[32] WANG P F, HAN Z. Friction and wear behaviors of a gradient nano-grained AISI 316L stainless steel under dry and oil-lubricated condition [J]. Journal of Materials Science and Technology, 2018, 34: 1835−1842.

[33] GODET M. Third-bodies in tribology [J]. Wear, 1990, 136: 29−45.

[34] SASADA T, OIKE M, EMORI N. The effect of abrasive grain size on the transition between abrasive and adhesive wear [J]. Wear, 1984, 97: 291−302.

[35] DILLAMORE I L. The stacking fault energy dependence of the mechanisms of deformation in FCC metals [J]. Metallurgical Transactions, 1970, 1: 2463−2470.

[36] SARMA V S, WANG J, JIAN W W, KAUFFMANN A, CONRAD H, FREUDENBERGER J, ZHU Y T. Role of stacking fault energy in strengthening due to cryo-deformation of FCC metals [J]. Materials Science and Engineering A, 2010, 527: 7624−7630.

[37] LIU X C, ZHANG H W, LU K. Formation of nanolaminated structure in an interstitial-free steel [J]. Scripta Materialia, 2015, 95: 54−57.

[38] MURR L E. Stacking-fault anomalies and the measurement of stacking-fault free energy in f.c.c. thin films [J]. Thin Solid Films, 1969, 4(6): 389−412.

[39] LIU Zhao-hua, CHEN Liang-wei, XI Jian, SHI Qing-nan. Dislocation refinement mechanism of high stacking fault energy 7003 Al alloy during ECAP deformation [J]. Rare Metal Materials and Engineering, 2013, 42: 1407−1410. (in Chinese)

[40] COHEN J B, WEERTMAN J. A dislocation model for twinning in f.c.c. metals [J]. Acta Metallurgica, 1963, 11: 996−998.

[41] WANG K, TAO N R, LIU G, LU J, LU K. Plastic strain-induced grain refinement at the nanometer scale in copper [J]. Acta Materialia, 2006, 54: 5281−5291.

[42] TAO N R, LU K. Nanoscale structural refinement via deformation twinning in face-centered cubic metals [J]. Scripta Materialia, 2009, 12: 1039−1043.

[43] TAO N R, ZHANG H W, LU J, LU K. Development of nanostructures in metallic materials with low stacking fault energies during surface mechanical attrition treatment (SMAT) [J]. Materials Transactions, 2003, 44: 1919−1925.

[44] YIN Cun-hong, LIANG Yi-long, JIANG Yun, YANG Ming, LONG Shao-lei. Formation of nano-laminated structures in a dry sliding wear-induced layer under different wear mechanisms of 20CrNi2Mo steel [J]. Applied Surface Science, 2017, 423: 305−313.

[45] KATO H, SASASE M, SUIYA N. Friction-induced ultra-fine and nanocrystalline structures on metal surfaces in dry sliding [J]. Tribology International, 2010, 43: 925−928.

[46] LIANG Shuang, ZHU Peng, YANG Yu-dan, HE Xing, WANG Wu-rong, WEI Xi-cheng. Subsurface dynamic deformation and nano-structural evolution in 40Cr steel under dry sliding wear [J]. Tribology Letters, 2019, 67: 1−9.

[47] QI Z, JIANG J, MELETIS E I. Wear mechanism of nanocrystalline Metals [J]. Journal of Nanoscience and Nanotechnology, 2009, 9: 4227−4232.

[48] ARCHARD J F. Contact and rubbing of flat surfaces [J]. Journal of Applied Physics, 1953, 24: 981−988.

[49] FARHAT Z N, DING Y, NORTHWOOD D O, ALPAS A T. Effect of grain size on friction and wear of nanocrystalline aluminum [J]. Materials Science and Engineering A, 1996, 206: 302−313.

[50] PRAKASH N A, GNANAMOORTHY R, KAMARAJ M. Friction and wear behavior of surface nanocrystallized aluminium alloy under dry sliding condition [J]. Materials Science and Engineering B, 2010, 168: 176−181.

[51] GE M Z, XIANG J Y, TANG Y, YE X, FAN Z, LU Y L, ZHANG X H. Wear behaviour of Mg−3Al−1Zn alloy subjected to laser shock peening [J]. Surface and Coatings Technology, 2018, 337: 501−509.

[52] LI Xiao-yan, LU Lei, LI Jiang-guo, ZHANG Xuan, GAO Hua-jian. Mechanical properties and deformation mechanisms of gradient nanostructured metals and alloys [J]. Nature Reviews Materials, 2020, 5: 706−723.

梯度纳米结构 Inconel 625 合金的形成机理及磨损行为

高钰璧 1,2,3，李秀艳 4，马元俊 1,2,4，Matthew KITCHEN3，丁雨田 1,2，罗全顺 3

1. 兰州理工大学 省部共建有色金属先进加工与再利用国家重点实验室，兰州 730050；
2. 兰州理工大学 材料科学与工程学院，兰州 730050；
3. Materials and Engineering Research Institute, Sheffield Hallam University, Sheffield, S1 1WB, UK；
4. 中国科学院 金属研究所 沈阳材料科学国家研究中心，沈阳 110016

摘　要：采用 SEM、TEM 和球盘式滑动磨损机研究梯度纳米结构(GNS) Inconel 625 合金的形成机理和磨损行为。结果表明，表面机械研磨处理(SMGT)诱导产生深度约为 800 μm 的梯度结构，其由表层纳米晶层、纳米层片层、纳米孪晶层和严重变形层组成，对应的显微硬度由 6.95 GPa (最表层)梯度降低到 2.77 GPa (粗晶基体)。同时，高密度纳米孪晶的形成以及随后的纳米孪晶与位错之间的交互作用导致纳米晶层的形成。经 SMGT 处理样品的 磨痕宽度和深度、磨损量和磨损率均小于未处理粗晶样品的；此外，两种样品的磨损机制主要是磨料磨损和粘着磨损，并伴有轻微的氧化磨损。GNS Inconel 625 合金耐磨性的显著增强归因于 GNS 表层具有高显微硬度、高残余压应力和高应变能力。

关键词：Inconel 625 合金；表面机械碾压处理；梯度纳米结构；形成机理；磨损行为；残余应力

(Edited by Wei-ping CHEN)